Study of plasmonic crystals using Fourier-plane images obtained with plasmon tomography far-field superlenses

R. Rodriguez,[1] C. J. Regan,[2,3] A. Ruiz-Columbié,[4] W. Agutu,[1] A. A. Bernussi,[2,3] and L. Grave de Peralta[1,3,a)]
[1]*Department of Physics, Texas Tech University, Lubbock, Texas 79409, USA*
[2]*Department of Electrical and Computer Engineering, Texas Tech University, Lubbock, Texas 79409, USA*
[3]*Nano Tech Center, Texas Tech University, Lubbock, Texas 79409, USA*
[4]*University College, Texas Tech University, Lubbock, Texas 79409, USA*

(Received 30 July 2011; accepted 20 September 2011; published online 24 October 2011)

We explore the use of surface plasmon polariton (SPP) tomography far-field superlenses for quantitative characterization of plasmonic crystals with sub-wavelength features. Essential information concerning the dependence of the effective refractive index on the hole diameter and the filling factor was obtained from the Fourier-plane images of the fabricated plasmonic crystals. We also provide a comprehensive discussion on the influence of hole diameters on the formation of directional stop-bands in plasmonic crystals. © *2011 American Institute of Physics*.
[doi:10.1063/1.3654001]

I. INTRODUCTION

The smallest feature size resolvable by conventional optical instruments is given by 0.61 λ/NA, where λ is the free space wavelength of the light and NA is the numerical aperture of the system.[1,2] In order to overcome the diffraction limit barrier, Pendry proposed in 2000 a near-field superlens based on a simple thin metal film that could be used for super-resolution imaging.[3] In addition to the search of superlenses, different approaches to achieve super-resolution imaging based on surface plasmon polariton (SPP) excitations[4,5] have been investigated.[6–8] The physics behind Pendry's near-field superlens relies on (1) light scattered by nanofeatures couples to evanescent waves that cannot be collected by the instrument's arrangement of lenses[9–12] and (2) the evanescent waves can be enhanced by a metal layer with an appropriate thickness.[13] Optical near-field[10] and far-field[11,12] superlenses have been already demonstrated. In those reports, the structures used to demonstrate far-field superlenses are much more complex than the simple thin metal layer proposed originally by Pendry. In particular, additional patterning of the metal was included in the superlens design to scatter the enhanced evanescent waves into the far-field.[11,12]

We have recently demonstrated[14] super-resolution images from dye-doped plasmonic crystals obtained by SPP tomography.[15–17] Nanofeatures with lateral dimensions smaller than λ/20 were resolved in the surface emission (SE) images.[14] In contrast to previous superlens designs, in our approach to achieve super-resolution imaging, the amplified evanescent waves are coupled to the far-field via SPP-coupled leakage radiation;[15] therefore no scattering features are required in our proposed superlens. In this work, we used Fourier-plane (FP) images from SPP tomography far-field superlenses to obtain quantitative information of plasmonic crystals with sub-wavelength features. We present simple semi-empirical relations describing the dependence of the plasmonic crystal effective refractive index on the crystal filling factor and the size of the holes. These semi-empirical relations are very useful for design and fabrication of plasmonic crystals with nanosize features. For instance, we show that the dependence of the hole size on the electron-beam dose used in the device fabrication can be directly obtained from the FP images. Finally, we present a comprehensive discussion about the formation of directional stop-bands[17] in the fabricated plasmonic crystals.

II. EXPERIMENTAL DETERMINATION OF THE SIZE OF THE HOLES

As illustrated in Fig. 1(a), dye-doped plasmonic crystals investigated here consist of periodic arrays of air holes defined on 150 nm thick dye-doped PMMA layer using electron-beam lithography technique. The PMMA layer was doped with Rhodamine 6G (R-6G), with peak emission at ~568 nm wavelength. The dye-doped PMMA layer was spun over a 50 nm thick gold film deposited on a glass substrate. The samples were investigated by plasmon tomography technique. Fig. 1(b) shows a sketch of our experimental set up. A CW laser pump source with emission centered at 532 nm wavelength was used for exciting the R-6G molecules in the top layer of the sample. Spontaneous emission photons emitted in all directions excite SPPs at the metal-PMMA interface. Radiation leaked to the sample substrate is collected by an immersion oil objective lens with high numerical aperture (NA = 1.49, 100×). A set of lenses, internal to the microscope body, perform magnification and image formation. Two charge-coupled device (CCD) cameras capture the FP and SE images. A bandpass filter with central wavelength at 568 nm was introduced after the immersion oil objective lens for filtering the SPP-coupled leakage radiation and blocking the direct excitation laser beam. Additional details of the experimental arrangement and sample fabrication can be found in Refs. 14–16.

Figure 2 shows SE and FP images of a plasmonic crystal fabricated with square lattice symmetry, period $p \sim 300$ nm,

[a)]Author to whom correspondence should be addressed. Electronic mail: luis.grave-de-peralta@ttu.edu.

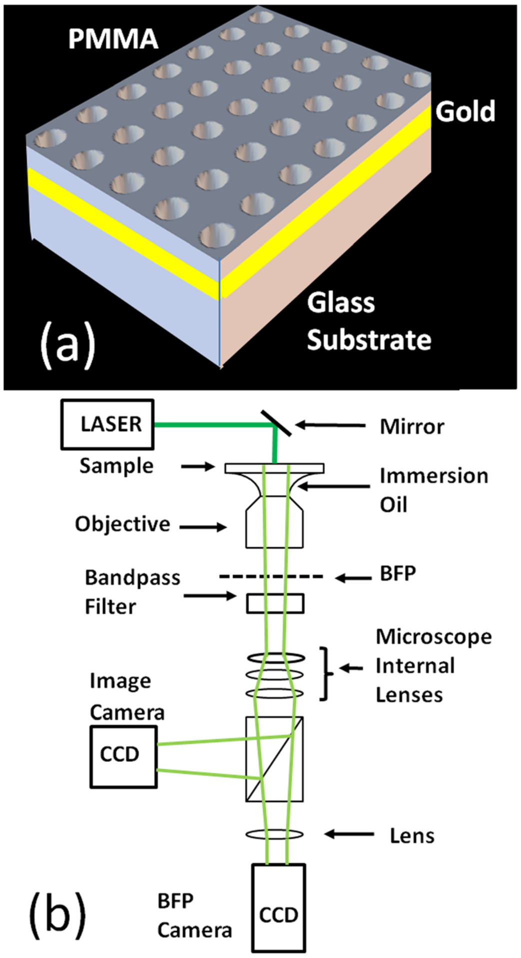

FIG. 1. (Color online) Illustrations of (a) structure of the fabricated samples and (b) plasmon tomography experimental set up.

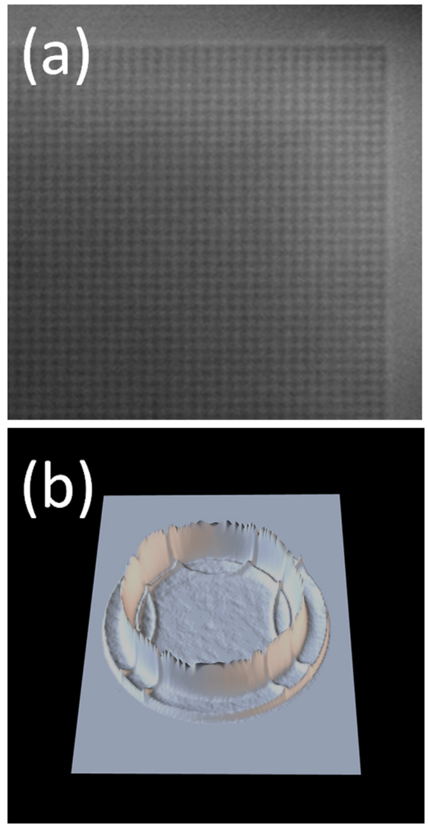

FIG. 2. (Color online) (a) SE and (b) FP images obtained with a SPP tomography superlens corresponding to a plasmonic crystal with square symmetry, $d \sim 100$ nm and $p \sim 300$ nm.

and holes with a diameter $d \sim 100$ nm. The patterned structure is clearly seen in the SE image shown in Fig. 2(a). The corresponding FP image is shown in Fig. 2(b), where the height is proportional to the light intensity in the three dimensional plot. The central prominent ring in the FP image corresponds to the excited SPP propagation mode with radius proportional to the magnitude of the wavevector $k_{spp} = 2\pi n_{eff}/\lambda$, where n_{eff} is the effective refractive index of the plasmon mode.[14,17] The larger outer background-disc corresponds to the high numerical aperture (NA = 1.49) of the collecting objective lens used in our experiments.[14,17] The prominence of the central rings compared to the background-disk is due to the extraordinary transmission through the thin gold layer of the SPP-coupled radiation.[13] This is a characteristic signature of occurrence of evanescent wave enhancement in thin metal film superlenses.[3,12] The ratio of the diameter of the central ring (d_r) to the diameter of the background disc (d_c) is equal to the ratio of the effective refractive index of the propagating mode to the numerical aperture of the collecting objective, i.e.,

$$n_{eff} = NA \frac{d_r}{d_c}. \tag{1}$$

Using this approach, we determined $n_{eff} \sim 1.15$ for the excited SPP mode in the crystal. The additional less intense arc segments shown in Fig. 2(b) are related to the symmetry and period of the crystal's lattice.[14,17] Therefore, in Fig. 2(b), the horizontal shift of the additional rings with respect to the central ring (s) is proportional to $2\pi/p$.[14–17] More explicitly

$$\frac{2\pi}{p} = \frac{2\pi}{\lambda} NA \frac{s}{d_c}. \tag{2}$$

Using this approach, we determined a value of $p \sim 296$ nm, which is in excellent agreement with the nominal fabrication value of $p = 300$ nm.

We fabricated several plasmonic crystals with square lattice symmetry, $p \sim 300$ nm and hole diameter varying from $d \sim 27-210$ nm. FP images were obtained for all the fabricated samples using the same SPP tomography far-field superlens arrangement. Effective refractive indexes were extracted from the FP images as described above. Fig. 3(a) shows the dependence of n_{eff} on the filling factor (F_f),[18] which is defined by the following formula

$$F_f = 1 - \frac{\pi d^2}{4p^2}. \tag{3}$$

A value $F_f = 1$ corresponds to no holes patterned on the PMMA layer while $F_f = 0$ corresponds to no PMMA layer deposited on top of the gold layer. The hole diameters shown in Fig. 3(a) correspond to averaged values measured, with a dispersion of ± 5 nm, using a scanning electron microscope

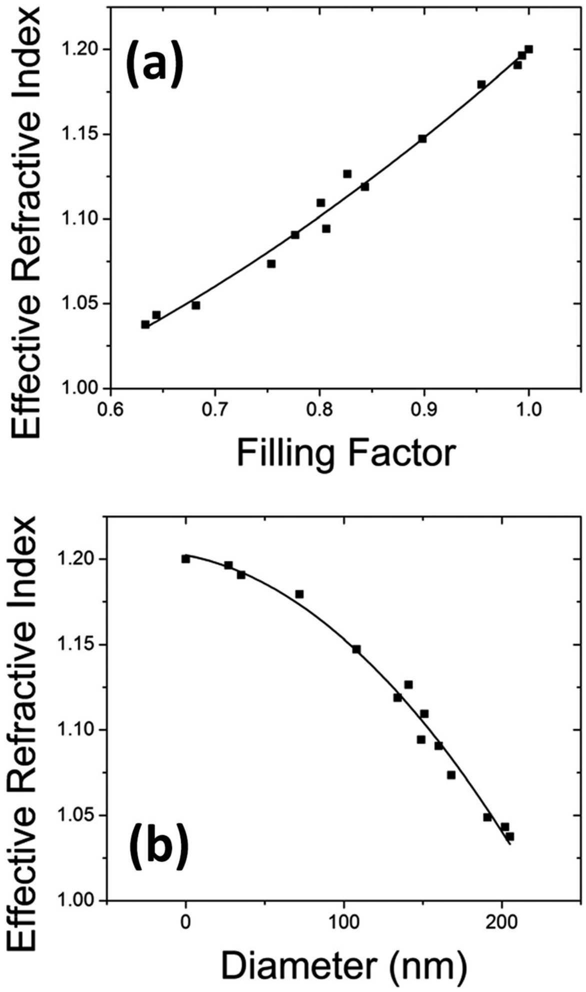

FIG. 3. Semi-empirical dependence (continuous curve) of the effective refractive index on (a) the fill factor and (b) the hole diameter. Determined for a plasmonic crystal with square symmetry and $p \sim 300$ nm. The squares are experimental points.

(SEM). The continuous curve in Fig. 3(a) corresponds to the following semi-empirical relation:[19]

$$n_{eff} = 1.2F_f + 1.02(1 - F_f) - \alpha F_f(1 - F_f). \qquad (4)$$

By fitting (4) to the experimental points, we determined a bowing coefficient of $\alpha \sim 0.4$. Fig. 3(b) shows the dependence of n_{eff} on the diameter of the holes. The continuous curve shown in Fig. 3(b) was calculated by substituting Eq. (3) in Eq. (4). An estimate of the sensitivity of this approach to the hole size can be obtained using Eq. (1) and the results shown in Fig. 3(b). For holes with diameter less (greater) than 100 nm, the ratio d_r/d_c decreases when the hole diameter increases at a rate of ~ -0.071 (-0.035)% per nm. For $d_c = 790$ pixels, this corresponds to a decrement in d_r at a rate of a pixel per a hole diameter increment of 3.6 (1.8) nm. FP images are easy to obtain and process; therefore, super-resolution capabilities of SPP tomography superlenses provides a practical alternative and/or complement to complex and time consuming simulations for plasmonic crystal design and fabrication. For instance, Fig. 4 shows the dependence of the size of the holes on the electron beam dose used to fabricate plasmonic crystals with a nominal hole diameter of $\sim$150 nm. The information contained in Fig. 4 is vital for the correct fabrication of the desired plasmonic crystal. The continuous curve in Fig. 4 corresponds to the non-linear least square fitting of the experimental points with a second-order polynomial. The electron beam dose corresponding to each fabricated plasmonic crystal was known while the values of n_{eff} were extracted from the corresponding FP images. Expressions (3) and (4) were used to convert refractive indexes into hole diameters.

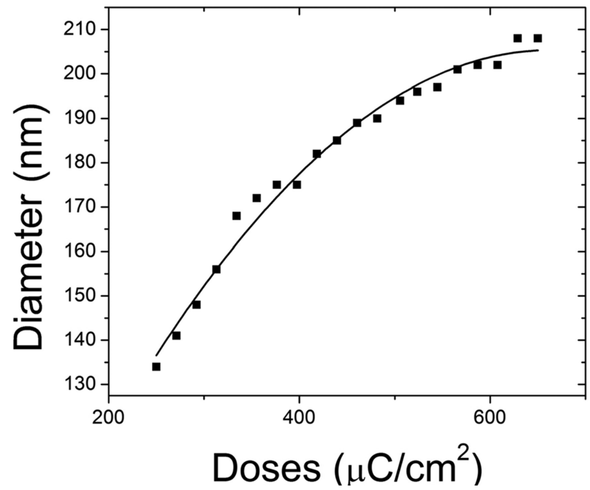

FIG. 4. Dependence of obtained hole diameter on the electron beam doses for a plasmonic crystal with square symmetry and $p \sim 300$ nm.

III. FORMATION OF DIRECTIONAL STOP-BANDS

Having a broad collection of FP images corresponding to plasmonic crystals with the same lattice symmetry and period, but with different sizes of the holes, allows us to experimentally study the influence of the diameter of the holes in the formation of directional stop-bands in the crystal. The dye molecules at the PMMA layer excited by the pump laser emit randomly, and thus some will evanescently couple to allow surface plasmon modes. For a uniform PMMA layer, SPP propagates in all directions. This corresponds to the emission of leakage radiation in a cone with angular magnitude corresponding to the SPP angle. However, the patterned periodic structure modifies how the photons propagate within a plasmonic crystal. Figures 5(a)–5(d) show FP images corresponding to plasmonic crystals with d $\sim$ 150, 170, 190, and 210 nm, respectively. It has been previously reported[17] that directional stop-bands are formed when the zero-order isofrequency dispersion ring (most prominent ring) intercepts the boundaries of the crystal first Brillouin zone (FBZ)[20] and in the directions where this ring is outside the FBZ. As shown in Fig. 5(d), this is the case for a plasmonic crystal with d $\sim$ 210 nm.[17] The deepest valleys in the FP images shown in Fig. 5 correspond to the four directional gaps that are formed where the FBZ intercept the most prominent ring.[17] Four well-defined directional stop-bands (indicated by arrows) are clearly seen in Fig. 5(d). However, the stop-bands are not well-defined in Figs. 5(a)–5(c). This indicates that well-defined directional stop-bands are only formed when the diameter of the holes are larger than $\sim$200 nm.

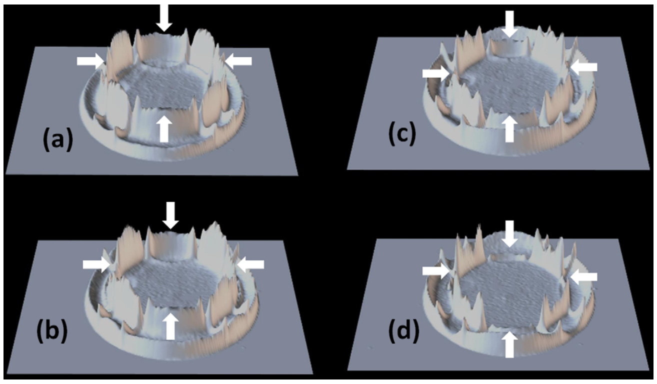

FIG. 5. (Color online) FP images illustrating the formation of the crystal stop bands. The diameter of the holes in the plasmonic crystal is (a) 150, (b) 170, (c) 190, and (d) 210 nm. Arrows point to the regions where directional stop-bands are formed.

Directional stop-bands are formed due to destructive interference of excited SPPs propagating in opposite directions in the crystal.[21] A well-defined directional stop-band corresponds to the formation of a standing wave in that particular direction of the crystal. As a result, no energy can flow in that direction. Complete cancelation of the amplitudes corresponding to SPPs excitations propagating in opposite directions of the crystals implies that SPPs are equally coupled to the first and zero-order isofrequency dispersion rings. This can only occur if the Rayleigh scattering produced by the patterned holes is sufficiently intense. The amplitude of the Rayleigh scattering is proportional to the sixth power of the diameter of the holes;[22] therefore, as suggested from the FP images shown in Figs. 2 and 5, the formation of well-defined directional stop-bands in a crystal strongly depend on the size of the holes. It is nonexistent for $d \sim 100$ nm (Fig. 2(b)) and it manifests completely in the narrow interval $170 < d \leq 210$ nm.

IV. CONCLUSIONS

We have explored the use of SPP tomography far-field superlenses for quantitative characterization of plasmonic crystals with sub-wavelength features. We described how to obtain, starting from the FP images, simple semi-empirical relations describing the dependence of the plasmonic crystal effective refractive index on the crystal filling factor and the size of the holes. These types of semi-empirical relations constitute a practical alternative and/or complement to time consuming sophisticated simulations for design and fabrication of plasmonic crystals. We also verified experimentally that well-defined directional stop-bands strongly depend on the size of the scattering centers. The results described in this work are important for fabricating plasmonic crystals to use in the generation of high in-plane collimated beams, realization of SPP cavities, and for sensing applications.

ACKNOWLEDGMENTS

This work was partially supported by the NSF CAREER Award (ECCS-0954490), U.S. Army CERDEC Contract (W15P7T-07-D-P040), and by the J. F. Maddox Foundation.

[1] M. Born and E. Wolf, *Principles of Optics*, 2nd ed. (Pergamon, New York, 1964).
[2] F. L. Pedrotti, L. S. Pedrotti, and L. M. Pedrotti, *Introduction to Optics*, 3rd ed. (Pearson Prentice Hall, New Jersey, 2007).
[3] J. B. Pendry, Phys. Rev. Lett. **85**, 3966 (2000).
[4] H. Raether, *Surface Plasmons on Smooth and Rough Surfaces and on Gratings* (Springer, Berlin, 1988).
[5] D. Sarid and W. Challener, *Modern Introduction to Surface Plasmons: Theory, Mathematica Modeling: Applications* (Cambridge University Press, 2010).
[6] V. K. Valev, A. V. Silhanek, Y. Jeyaram, D. Denkova, B. De Clercq, V. Petkov, X. Zheng, V. Volskiy, W. Gillijns, G. A. E. Vandenbosch, O. A. Aktsipetrov, M. Ameloot, V. V. Moshchalkov, and T. Verbiest, Phys. Rev. Lett. **106**, 226803 (2011).
[7] A. McLeod, A. Weber-Bargioni, Z. Zhang, S. Dhuey, B. Harteneck, J. B. Neaton, S. Cabrini, and P. J. Schuck, Phys. Rev. Lett. **106**, 037402 (2011).
[8] A. Alù and N. Engheta, Phys. Rev. Lett. **105**, 263906 (2011).
[9] J. W. Goodman, *Introduction to Fourier Optics* (McGraw-Hill, New York, 1968).
[10] D. O. S. Melville and R. J. Blaikie, Opt. Express **13**, 2127 (2005).
[11] Z. Liu, S. Durant, H. Lee, Y. Pikus, Y. Xiong, C. Sun, and X. Zhang, Opt. Express **15**, 6947 (2007).
[12] X. Zhang and Z. Liu, Nature Mater. **7**, 435 (2008).
[13] Z. Liu, N. Fang, T. Yen, and X. Zhang, Appl. Phys. Lett. **83**, 5184 (2003).
[14] R. Rodriguez, W. Agutu, C. J. Regan, A. Ajimo, A. A. Bernussi, and L. Grave de Peralta, "Far-field superlenses based dye-doped plasmonic crystals," AIP Advances (to be published).
[15] S. P. Frisbie, C. F. Chesnutt, M. E. Holtz, A. Krishnan, L. Grave de Peralta, and A. A. Bernussi, IEEE Photon. J. **1**, 153 (2009).
[16] L. Grave de Peralta, R. Lopez-Boada, A. Ruiz-Columbie, S. Park, and A. A. Bernussi, J. Appl. Phys. **109**, 023101 (2011).
[17] C. J. Regan, A. Krishnan, R. Lopez-Boada, L. Grave de Peralta, and A. A. Bernussi, Appl. Phys. Lett. **98**, 151113 (2011).
[18] E. Devaux, J. Y. Laluet, B. Stein, C. Genet, T. Ebbesen, J. C. Weeber, and A. Dereux, Opt. Express **18**, 20615 (2010).
[19] A. Rockett, *The Materials Science of Semiconductors* (Springer, New York, 2008).
[20] C. Kittel, *Introduction to Solid State Physics*, 7th ed. (Wiley, New York, 1996).
[21] A. Giannattasio and W. L. Barnes, Opt. Express **13**, 428 (2005).
[22] A. J. Cox, A. J. DeWeerd, and J. Linden, Am. J. Phys. **70**, 621 (2002).